

Orbital polarization, charge transfer, and fluorescence in reduced-valence nickelates

M. R. Norman ^{1,*}, A. S. Botana ², J. Karp,³ A. Hampel ⁴, H. LaBollita,^{2,4} A. J. Millis ^{4,5},
G. Fabbri ⁶, Y. Shen ⁷ and M. P. M. Dean ⁷¹Materials Science Division, Argonne National Laboratory, Lemont, Illinois 60439, USA²Department of Physics, Arizona State University, Tempe, Arizona 85287, USA³Department of Applied Physics and Applied Math, Columbia University, New York, New York 10027, USA⁴Center for Computational Quantum Physics, Flatiron Institute, 162 5th Avenue, New York, New York 10010, USA⁵Department of Physics, Columbia University, New York, New York 10027, USA⁶Advanced Photon Source, Argonne National Laboratory, Lemont, Illinois 60439, USA⁷Condensed Matter Physics and Materials Science Department, Brookhaven National Laboratory, Upton, New York 11973, USA

(Received 17 February 2023; revised 27 March 2023; accepted 29 March 2023; published 12 April 2023)

This paper presents a simple formalism for calculating x-ray absorption (XAS) and resonant inelastic x-ray scattering (RIXS) that has as input orbital-resolved density of states from a single-particle or many-body *ab initio* calculation and is designed to capture itinerant like features. We use this formalism to calculate both the XAS and RIXS with input from density functional theory (DFT) and DFT + DMFT for the recently studied reduced valence nickelates $R_4\text{Ni}_3\text{O}_8$ and RNiO_2 ($R = \text{rare earth}$), and these results are then contrasted with those for the cuprate CaCuO_2 and the unreduced nickelate $R_4\text{Ni}_3\text{O}_{10}$. In contrast to the unreduced $R_4\text{Ni}_3\text{O}_{10}$, the reduced valence nickelates as well as the cuprate show strong orbital polarization due to the dominance of $x^2 - y^2$ orbitals for the unoccupied $3d$ states. We also reproduce two key aspects of a recent RIXS experiment for $R_4\text{Ni}_3\text{O}_8$: (i) a charge-transfer feature between $3d$ and oxygen $2p$ states whose energy we find to decrease as one goes from RNiO_2 to $R_4\text{Ni}_3\text{O}_8$ to the cuprate, and (ii) an energy-dependent polarization reversal of the fluorescence line that arises from hybridization of the unoccupied $3z^2 - r^2$ states with R $5d$ states. We end with some implications of our results for the nature of the $3d$ electrons in reduced valence nickelates.

DOI: [10.1103/PhysRevB.107.165124](https://doi.org/10.1103/PhysRevB.107.165124)

I. INTRODUCTION

Since the discovery of superconductivity in Sr-doped NdNiO_2 in 2019 [1], there has been an active debate about the nature of reduced valence nickelates and how they compare to the cuprates. An important question has been the placement of the materials on the charge-transfer Mott continuum defined by Zaanen *et al.* [2]. Recent studies [3] suggest that the reduced nickelates are intermediate between the charge transfer and Mott limits, though the Mott limit is often assumed. The configuration of the Ni $3d$ states, in particular whether the $3z^2 - r^2$ states are partially filled, is also of interest. These questions have been difficult to resolve experimentally and also less straightforward to treat in theory.

X-ray absorption spectroscopy (XAS) and resonant inelastic x-ray scattering (RIXS) have been instrumental in addressing these matters, and such studies exist for RNiO_2 ($R = \text{rare earth}$) and its hole-doped variant (with a formal d count of $9 - x$, where x is the hole doping gotten by partially replacing R by Sr), as well as for the stoichiometric reduced Ruddlesden-Popper phases $R_4\text{Ni}_3\text{O}_8$ (with a formal d count of 8.67). Various x-ray edges have been studied. Here, we focus on the nickel L edge since it directly involves the $3d$ electrons,

and specifically the L_2 edge since the L_3 edge overlaps with the La M_4 edge.

$d-d$ excitations, prominent in the cuprates, dominate the RIXS in these nickelates in the range of 1–2 eV [4–6] but we do not focus on these local excitations here. Rather, the RIXS spectra above 2 eV are dominated by (i) a charge-transfer feature and (ii) a fluorescence line. It is these features we are interested in addressing in this paper. To accomplish this goal, we present a simple formalism that takes as input orbital-resolved density of states (DOS) from a single-particle or many-body *ab initio* calculation. We then calculate the RIXS and XAS spectra from the joint density of states by including polarization matrix elements of these states with the core hole.

(i) We find that the higher energy s -polarized feature in the RIXS loss spectrum near zero incident energy (relative to the Fermi energy [7]) correlates with the charge-transfer energy between nickel $3d$ and oxygen $2p$ electrons, as observed in $R_4\text{Ni}_3\text{O}_8$ [6]. (ii) We find that the fluorescence line (a diagonal in energy feature in the incident energy–loss energy plane) crosses over as a function of incident energy from s polarization dominated (due to a strong signal from unoccupied $x^2 - y^2$ electrons) to p polarization dominated (due to a weaker signal from unoccupied $3z^2 - r^2$ electrons), again in agreement with the recent RIXS measurement for $R_4\text{Ni}_3\text{O}_8$ [6]. This is corroborated by XAS, which we also calculate. These unoccupied $3z^2 - r^2$ electrons are dispersive due to their hybridization with the R $5d$ states. We find similar

*norman@anl.gov

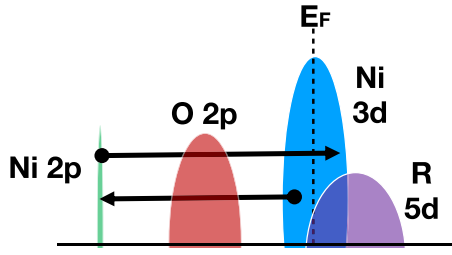


FIG. 1. Illustration of L edge RIXS for the nickelates in the approximation used in this paper. The upper arrow denotes excitation from the Ni $2p$ core electrons to the unoccupied Ni $3d$ states; the lower arrow denotes deexcitation from an occupied Ni $3d$ state that fills the Ni $2p$ core hole left from the first process. The analogous XAS process only involves the upper arrow. Here, E_F denotes the Fermi energy.

behavior for CaCuO_2 due to mixing of $\text{Cu } 3z^2 - r^2$ with the unoccupied Ca $3d$ states. We contrast this behavior with unreduced $\text{La}_4\text{Ni}_3\text{O}_{10}$ (with a formal d count of 7.33), where little polarization contrast is seen in the fluorescence line due to the weak orbital polarization associated with the unoccupied $3d-e_g$ states. Again, this is consistent with recent RIXS results mentioned below.

In Sec. II, we present our formalism, and in Sec. III, our results. We end in Sec. IV with implications of our work.

II. METHODS

Figure 1 illustrates the RIXS L edge process, in which an initial excitation of an electron from an atomic core Ni $2p$ state to an unoccupied Ni $3d$ state is followed by a transition from an occupied Ni $3d$ state to the hole in the Ni $2p$ shell. Following previous work [8], we model this in terms of the joint density of states of empty and filled states; however, unlike Ref. [8], we include polarization matrix elements of the valence/conduction electrons with the core hole. This particle-hole approximation is designed to capture more itinerant like features such as the fluorescence line. The resulting RIXS cross section, derived from the underlying Kramers-Heisenberg formalism [8,9] as shown in the Appendix, is

$$\bar{\sigma}(E_{\text{in}}, E_{\text{out}}, \epsilon) = \sum_{i,f,\sigma,\sigma',\epsilon'} \int dE \rho_{f\sigma'}(E) \rho_{i\sigma}(E + E_{\text{loss}}) \times \frac{\Gamma}{2} \frac{M_{if\sigma\sigma'}(\epsilon, \epsilon')}{(E - E_{\text{out}})^2 + \Gamma^2/4}, \quad (1)$$

where $\rho_{i\sigma}$ is the unoccupied Ni $3d$ DOS for orbital i and spin σ , $\rho_{f\sigma'}$ is the same but for occupied states, and the energy integral is over the occupied $3d$ states such that $E + E_{\text{loss}} > E_F$ where E_F is the Fermi energy, E_{in} the incident energy, E_{out} the outgoing energy, and E_{loss} the loss energy ($E_{\text{in}} - E_{\text{out}}$), with Γ the core-hole broadening. Implicit in this formula is a sum over Ni sites. Of central importance are the polarization matrix elements between the valence/conduction states and the core holes that in the dipole approximation are

$$M_{if\sigma\sigma'}(\epsilon, \epsilon') = \left| \sum_j \langle f\sigma' | \epsilon' | j \rangle \langle j | \epsilon | i\sigma \rangle \right|^2, \quad (2)$$

where ϵ, ϵ' are the incoming and outgoing photon polarizations, and j are the core states (two $2p_{\pm 1/2}$ states for L_2). For the core-conduction/valence matrix elements, we only include the angular and spin factors, as the radial factors are just an overall constant (since our results are based on band structure codes, the radial factors for all the $3d$ atomic basis orbitals associated with the muffin tins are the same). The angular integrals are Gaunt coefficients. Assuming the surface normal z is along c , the electric fields are

$$\begin{aligned} E_x &= (Y_{1-1} - Y_{11})/\sqrt{2}, \\ E_y &= i(Y_{1-1} + Y_{11})/\sqrt{2}, \\ E_z &= Y_{10}, \end{aligned} \quad (3)$$

where Y_{LM} are spherical harmonics, giving rise to the polarizations

$$\begin{aligned} s, s' &= \sin \phi E_x - \cos \phi E_y, \\ p &= \cos \theta E_z + \sin \theta (\cos \phi E_x + \sin \phi E_y), \\ p' &= \cos \theta' E_z + \sin \theta' (\cos \phi E_x + \sin \phi E_y), \end{aligned} \quad (4)$$

where θ is the incoming angle relative to the xy plane, θ' is minus the outgoing angle relative to the xy plane ($2\Theta_{sc} = \theta - \theta'$), and ϕ is the rotation angle within the xy plane. Given these expressions for ϵ and ϵ' , the Gaunt coefficients are then easily determined by the following angular decompositions of the core states for L_2 :

$$\begin{aligned} 2p_{1/2} &= (\sqrt{2}Y_{11} \downarrow - Y_{10} \uparrow)/\sqrt{3}, \\ 2p_{-1/2} &= (\sqrt{2}Y_{1-1} \uparrow - Y_{10} \downarrow)/\sqrt{3} \end{aligned}$$

and the $3d$ states

$$\begin{aligned} xy &= i(Y_{2-2} - Y_{22})/\sqrt{2}, \\ x^2 - y^2 &= (Y_{2-2} + Y_{22})/\sqrt{2}, \\ xz &= (Y_{2-1} - Y_{21})/\sqrt{2}, \\ yz &= i(Y_{2-1} + Y_{21})/\sqrt{2}, \\ 3z^2 - r^2 &= Y_{20}. \end{aligned}$$

In the above formalism, we sum over outgoing polarizations s' and p' , and so present results for either incoming s or incoming p .

Similarly, we can calculate the XAS [10]:

$$\bar{\sigma}(E_{\text{in}}, \epsilon) = \sum_{i,\sigma} \int dE \frac{\Gamma}{2} \frac{\rho_{i\sigma}(E) M_{i\sigma}(\epsilon)}{(E_{\text{in}} - E)^2 + \Gamma^2/4} \quad (5)$$

with

$$M_{i\sigma}(\epsilon) = \left| \sum_j \langle i\sigma | \epsilon | j \rangle \right|^2 \quad (6)$$

and the energy integral is over the unoccupied $3d$ states.

The above formalism has been designed for ease and generality of use and can take as input any calculation that provides an orbitally resolved DOS. A limitation of the formalism in its present form is that it does not take into account the interaction of the excited electron with the core hole, and so cannot describe Raman-like features such as $d-d$ excitations; however, we observe that it can be generalized

to do so if one derives the DOS from a supercell with a core hole on the absorbing site as recently demonstrated for osmates [11].

For input, we use previously published density functional theory (DFT) results for LaNiO_2 [12], CaCuO_2 [12], $\text{La}_4\text{Ni}_3\text{O}_8$ [13], and $\text{La}_4\text{Ni}_3\text{O}_{10}$ [14], and dynamical mean-field theory (DFT + DMFT) results for NdNiO_2 [15,16], CaCuO_2 [15,16], and $\text{Pr}_4\text{Ni}_3\text{O}_8$ [16]. In all cases, the $4f$ electrons were treated as core electrons, and so the choice of the rare-earth ion is not important for the purposes of this paper. For Γ , we assume 0.6 eV appropriate for the Ni L_2 edge [6]. Since the inputs we use have tetragonal symmetry, the results are independent of ϕ . DOS are in states per eV per Ni. Although the presented RIXS and XAS cross sections are only proportional (because of the radial matrix elements), all calculations use the same normalization (and are per Ni ion).

III. RESULTS

We first consider $R_4\text{Ni}_3\text{O}_8$. This trilayer nickelate (one inner NiO_2 plane, two outer NiO_2 planes) is reduced from its parent Ruddlesden-Popper phase $R_4\text{Ni}_3\text{O}_{10}$ by removal of its apical oxygens and has a formal $3d$ count of 8.67, making it analogous to overdoped cuprates. An advantage of these 438 trilayer nickelates is that good quality bulk single crystals exist [17,18], unlike the infinite-layer 112 nickelates where thin film growth is required, enabling a wider range of experiments including high-quality RIXS data [6].

To begin our analysis, we show in Fig. 2(a) the DFT-derived nickel $3d$ orbitally resolved DOS for the outer Ni planes of $\text{La}_4\text{Ni}_3\text{O}_8$ (the ones for the inner plane are similar). Near the Fermi level, the dominant DOS is that of the $x^2 - y^2$ states that extends from about 1 eV below E_F to about 2 eV above. We also note the occupied feature about 5 eV below E_F which is due to mixing between the Ni $x^2 - y^2$ and the oxygen $2p\sigma$ states. The other $3d$ states (t_{2g} and $3z^2 - r^2$) form sharp localized-like states below E_F , though $3z^2 - r^2$ has a weaker unoccupied part that is broad in energy due to mixing with the R $5d$ electrons. Figure 2(b) shows the same density of states, but now calculated using the DFT + DMFT method. The general features are similar; however, the $x^2 - y^2$ spectrum is broadened in energy due to correlations.

We now show how this DOS is reflected in the RIXS and XAS. Figures 2(c) and 2(d) show the RIXS spectra in the incident energy–loss energy plane at the L_2 edge for $\text{La}_4\text{Ni}_3\text{O}_8$ calculated using the DFT density of states shown in Fig. 2(a). The scattering angle ($2\Theta_{sc} = 153^\circ$) was chosen to agree with that of Ref. [6]. The left plot is for s polarization and the right plot for p polarization. The most prominent feature in these plots is a diagonal feature which is the fluorescence line, with this diagonal behavior typical of itinerant like states (d - d excitations, on the other hand, occur at a specific loss energy). At energies below 3 eV or so, the line is dominantly s polarized; for energies above this, it is dominantly p polarized. This is seen in experiment [6] as shown in Figs. 2(g) and 2(h) [19]. Given that the unoccupied $3d$ states are either $x^2 - y^2$ or $3z^2 - r^2$ [Fig. 2(a)], we redid the calculations restricting the initial states i in Eq. (1) to either one of these orbitals. As expected, the s signal arises from the $x^2 - y^2$ states and the p

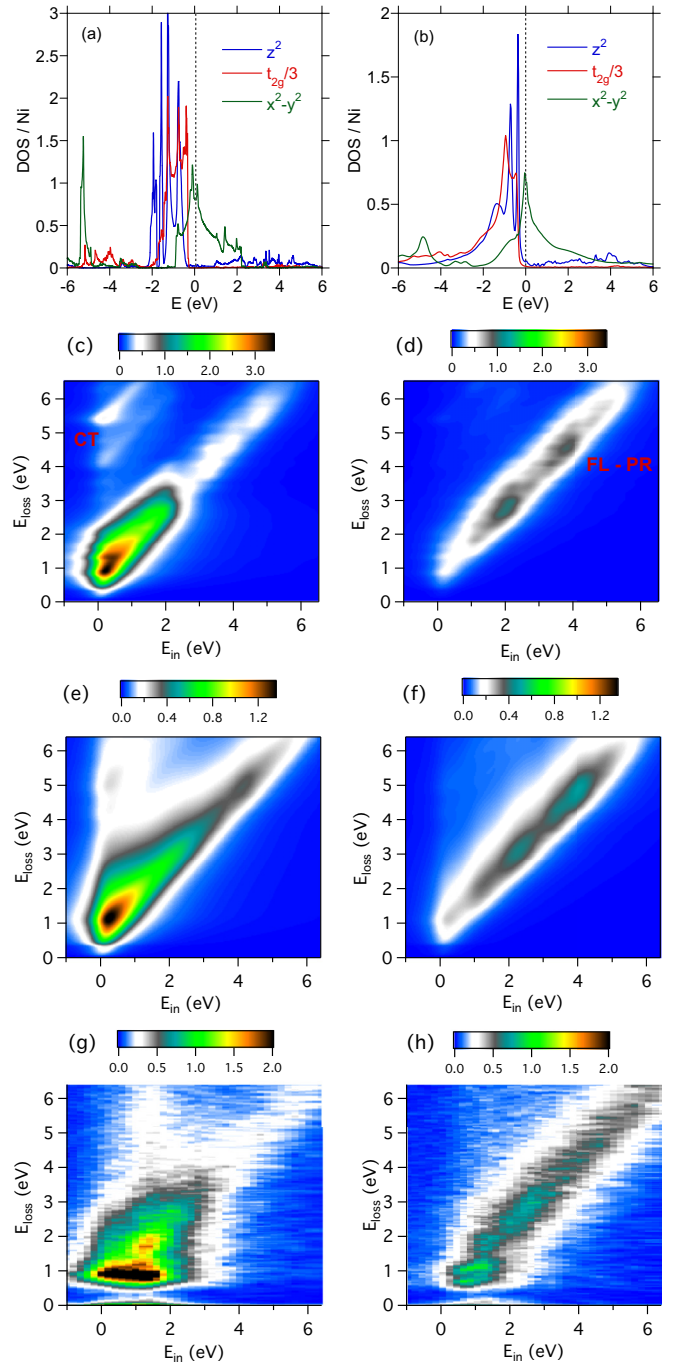


FIG. 2. Density of states for $R_4\text{Ni}_3\text{O}_8$ for the outer Ni planes from (a) DFT ($R = \text{La}$) and (b) DFT + DMFT ($R = \text{Pr}$). The ones for the inner Ni planes are similar. RIXS spectra for $\text{La}_4\text{Ni}_3\text{O}_8$ from DFT for s polarization (c) and p polarization (d). CT denotes the charge-transfer feature, and FL-PR the polarization reversal of the fluorescence line. RIXS spectra for $\text{Pr}_4\text{Ni}_3\text{O}_8$ from DFT + DMFT for s polarization (e) and p polarization (f). RIXS data for $\text{La}_4\text{Ni}_3\text{O}_8$ for s polarization (g) and p polarization (h) from Ref. [6], replotted as described in the text. For (c)–(h), $\theta = 15^\circ$ and $2\Theta_{sc} = 153^\circ$.

signal from the $3z^2 - r^2$ states. The stronger overall intensity of the s signal is due to the dominance of $x^2 - y^2$ in the near E_F region. The contribution from unoccupied $3z^2 - r^2$ states is more spread out in energy, a reflection of their hybridization

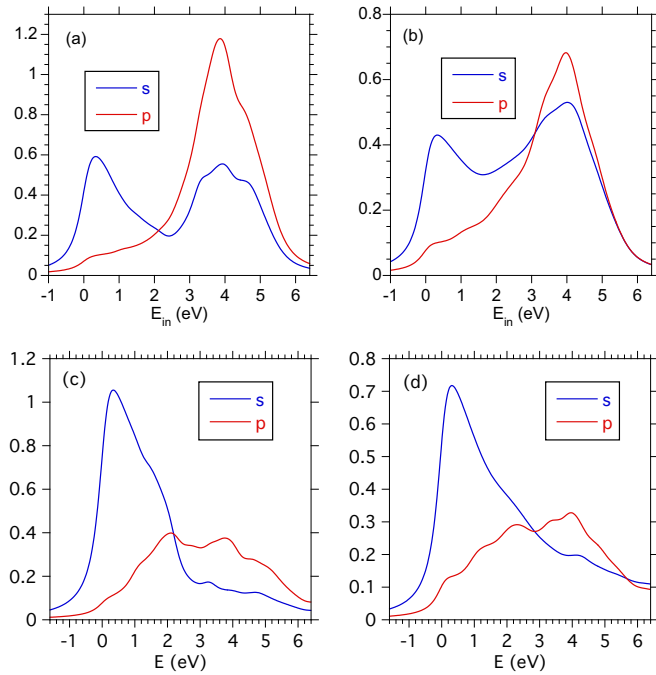


FIG. 3. Integration of RIXS spectra for $R_4\text{Ni}_3\text{O}_8$ from 4 to 6 eV loss from DFT [(a) $R = \text{La}$ from Figs. 2(c) and 2(d)] and from DFT + DMFT [(b) $R = \text{Pr}$ from Figs. 2(e) and 2(f)]. XAS for $R_4\text{Ni}_3\text{O}_8$ from DFT [(c) $R = \text{La}$] and from DFT + DMFT [(d) $R = \text{Pr}$] with $\theta = 15^\circ$.

with the dispersive R $5d$ states. This is evident as well from previous RIXS simulations of $R\text{NiO}_2$ where the fluorescence line was suppressed by artificially turning off the Ni $3d$ – R $5d$ hybridization [20]. The feature near zero incident energy and E_{loss} around 4–6 eV is s polarized and is due to charge-transfer excitations between $x^2 - y^2$ and oxygen $2p\sigma$ states as mentioned before in connection with the DOS in Fig. 2(a). This feature is also seen in experiment [6] as shown in Figs. 2(g) and 2(h).

Figures 2(e) and 2(f) show the s - and p -polarized spectra computed using the DFT + DMFT density of states. The features are similar to those obtained in the DFT calculation; the quantitative differences can be traced to the renormalization of the $3d$ states due to correlations for DMFT [Fig. 2(b)]. This is particularly seen for the charge-transfer feature near zero incident energy and E_{loss} larger than 3 eV. In fact, these DMFT results more closely resemble the experimental data as can be seen by comparing Figs. 2(e) and 2(f) to Figs. 2(g) and 2(h).

The DFT and DMFT calculations only partially succeed in mirroring the data from Figs. 2(g) and 2(h) in the range of 1–2 eV loss. This is because our formalism is not designed to capture the Raman-like d - d features that arise from the tendency of the core-hole potential well on the Ni sites in the intermediate RIXS state to localize the $3d$ states. We refer to Ref. [6] for a detailed discussion of cluster calculations that do account for these d - d excitations.

To investigate further, similar to Ref. [6], we integrate the RIXS spectra from 4 to 6 eV in energy loss and plot as a function of incident energy in Figs. 3(a) (DFT) and 3(b) (DFT + DMFT). For both calculations, one sees that that

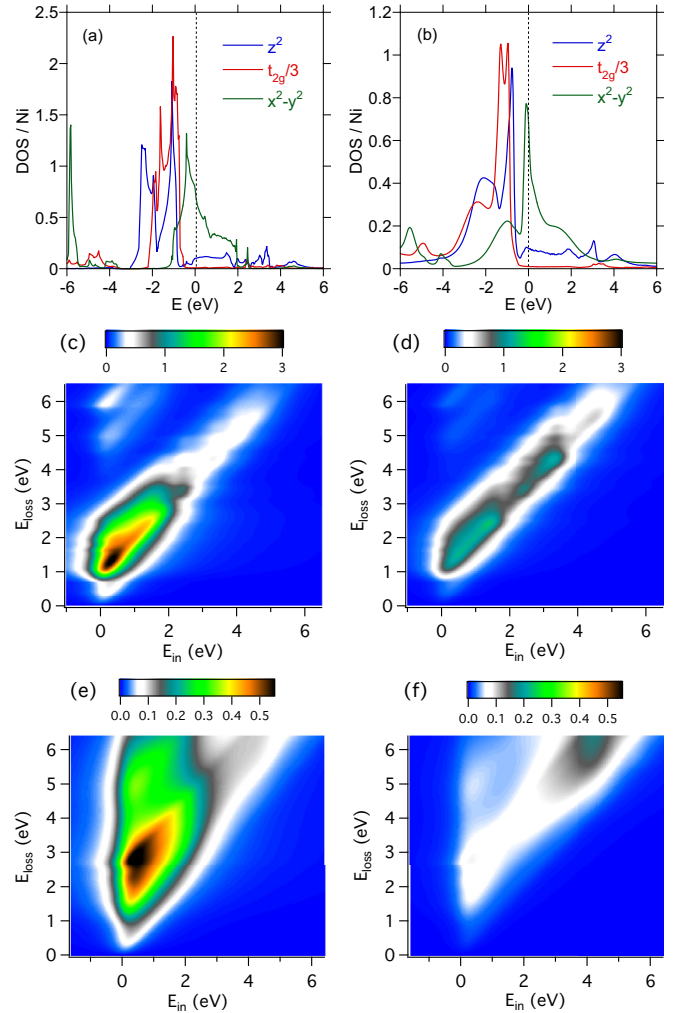


FIG. 4. Density of states for $R\text{NiO}_2$ from DFT [(a) $R = \text{La}$] and DFT + DMFT [(b) $R = \text{Nd}$]. RIXS spectra for LaNiO_2 from DFT for s polarization (c) and p polarization (d). RIXS spectra for NdNiO_2 from DFT + DMFT for s polarization (e) and p polarization (f). For (c)–(f), $\theta = 15^\circ$ and $2\theta_{\text{sc}} = 153^\circ$.

the lower incident energy part is dominantly s polarized (the charge-transfer feature), with the higher incident energy part strongly (DFT) or more modestly (DFT + DMFT) p polarized (the fluorescence line), as in the experiment [Fig. 2(d) of Ref. [6]]. The basic message of Figs. 2 and 3 is also reflected in the XAS [Figs. 3(c) and 3(d)] which again reflect a strong s polarization at low energies and a more moderate p polarization at higher energies. The strong orbital polarization of the XAS, similar to that of the cuprates, has already been remarked on in previous work [18].

Similar behavior is predicted for (undoped) $R\text{NiO}_2$ (Figs. 4 and 5), though with more differences for the DFT + DMFT RIXS spectra. The fluorescence line is also quite prominent in the RIXS data [4,5], though the charge-transfer feature is not so evident (though the more recent data of Ref. [5] only extended up to a 4 eV loss). We can contrast this with the cuprate CaCuO_2 (Figs. 6 and 7). Although the behavior is as well similar, there are some significant differences due to the fact that the Ca $3d$ states (the analogs of the R $5d$ states) are pushed

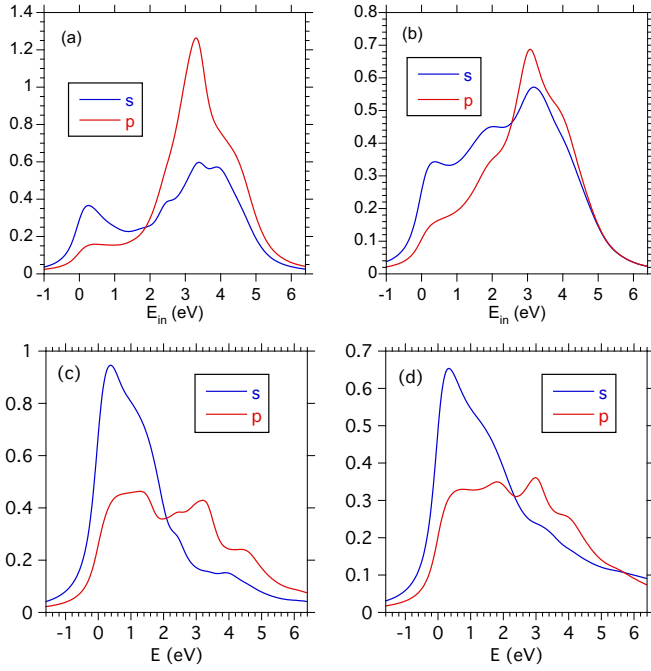


FIG. 5. Integration of RIXS spectra for $R\text{NiO}_2$ from 4 to 6 eV loss from DFT [(a) $R = \text{La}$ from Figs. 4(c) and 4(d)] and from DFT + DMFT [(b) $R = \text{Nd}$ from Figs. 4(e)–4(f)]. XAS for $R\text{NiO}_2$ from DFT [(c) $R = \text{La}$] and from DFT + DMFT [(d) $R = \text{Nd}$] with $\theta = 15^\circ$.

upwards in energy by about 2 eV and the charge-transfer energy for the cuprates is about 2 eV lower. It is the latter that makes the cuprates more charge-transfer-like (doped holes sitting mostly on the oxygen sites but with appreciable nickel character) as compared to the more Mott-like behavior of the reduced valence nickelates (doped holes sitting mostly on the nickel sites but with appreciable oxygen character). Unfortunately, almost all RIXS data on cuprates concentrate on lower energy features, though both the charge transfer and the fluorescence line have been observed in $\text{Ca}_2\text{CuO}_2\text{Cl}_2$ [21,22]. Comparing all of the figures, it becomes evident that $R_4\text{Ni}_3\text{O}_8$ is intermediate in behavior between $R\text{NiO}_2$ and CaCuO_2 . This is a reflection of their charge-transfer energies, that is smallest for the cuprate and largest for the undoped infinite-layer nickelate, with the difference between $R\text{NiO}_2$ and $R_4\text{Ni}_3\text{O}_8$ mostly due to their difference in doping.

The above can in turn be contrasted with the results on $R_4\text{Ni}_3\text{O}_{10}$ shown in Fig. 8 [23]. These results indicate little orbital polarization (the s and p signals are very similar). For XAS, this has been previously reported [18], but RIXS intensity plots in the incident energy–energy loss plane verify this [24]. This is because the formal $3d$ count of these unreduced nickelates is 7.33, meaning the unoccupied $3d$ states have both strong $x^2 - y^2$ and $3z^2 - r^2$ character. We further illustrate this by showing in Table I the unoccupied spectral weight for $x^2 - y^2$ and $3z^2 - r^2$ orbitals from the DOS plots as a representation of the orbital polarization. Consistent with the trends discussed in this section, the $3z^2 - r^2$ unoccupied weight increases as one goes from CaCuO_2 to $R_4\text{Ni}_3\text{O}_8$ to $R\text{NiO}_2$ to $R_4\text{Ni}_3\text{O}_{10}$.

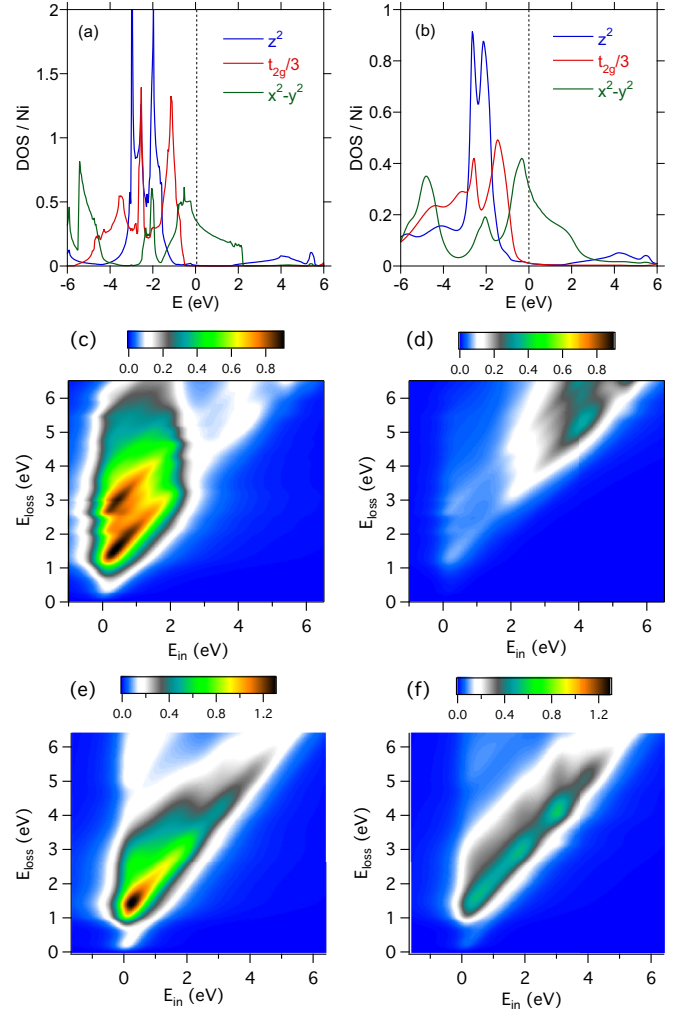


FIG. 6. Density of states for CaCuO_2 from DFT (a) and DFT + DMFT (b). RIXS spectra for CaCuO_2 from DFT for s polarization (c) and p polarization (d). RIXS spectra for CaCuO_2 from DFT + DMFT for s polarization (e) and p polarization (f). For (c)–(f), $\theta = 15^\circ$ and $2\Theta_{sc} = 153^\circ$.

IV. SUMMARY

In this paper, we presented a simple formalism for calculating RIXS fluorescence lines and other related features that are of an itinerant like nature, and used this to address RIXS data

TABLE I. Unoccupied spectral weight for $x^2 - y^2$ and $3z^2 - r^2$ orbitals from the density of states plots shown in the paper. The first column for each orbital is the DFT results and the second column the DFT+DMFT results. For the second row, $R = \text{La}$ for DFT and $R = \text{Pr}$ for DMFT. For the third row, $R = \text{La}$ for DFT and $R = \text{Nd}$ for DMFT.

	$3z^2 - r^2$		$x^2 - y^2$	
CaCuO_2	0.20	0.16	0.52	0.51
$R_4\text{Ni}_3\text{O}_8$	0.36	0.34	0.92	0.93
$R\text{NiO}_2$	0.42	0.40	0.77	0.83
$\text{La}_4\text{Ni}_3\text{O}_{10}$	0.76	0.84		

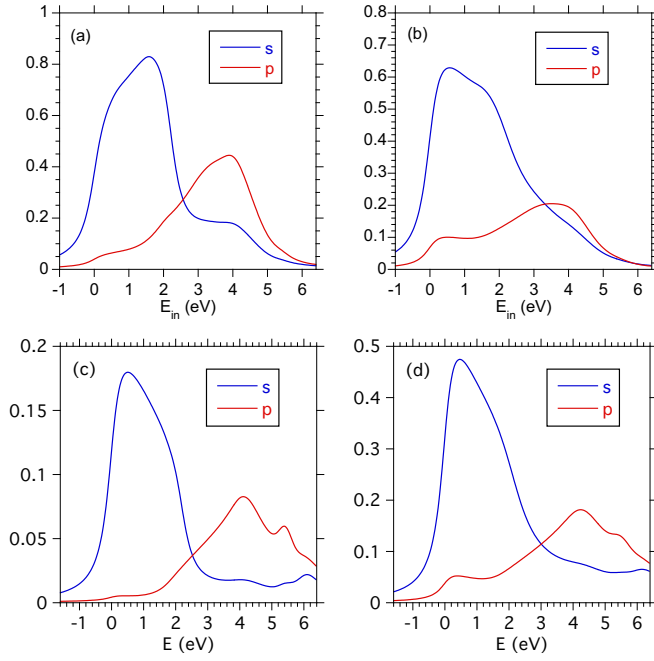


FIG. 7. Integration of RIXS spectra for CaCuO_2 from 4 to 6 eV loss from DFT [(a) from Figs. 6(c) and 6(d)] and from DFT + DMFT [(b) from Figs. 6(e) and 6(f)]. XAS for CaCuO_2 from DFT (c) and from DFT + DMFT (d) with $\theta = 15^\circ$.

on reduced valence nickelates. In these simulations, we identify charge-transfer features near zero incident energy, and a polarization reversal of the fluorescence line as a function of

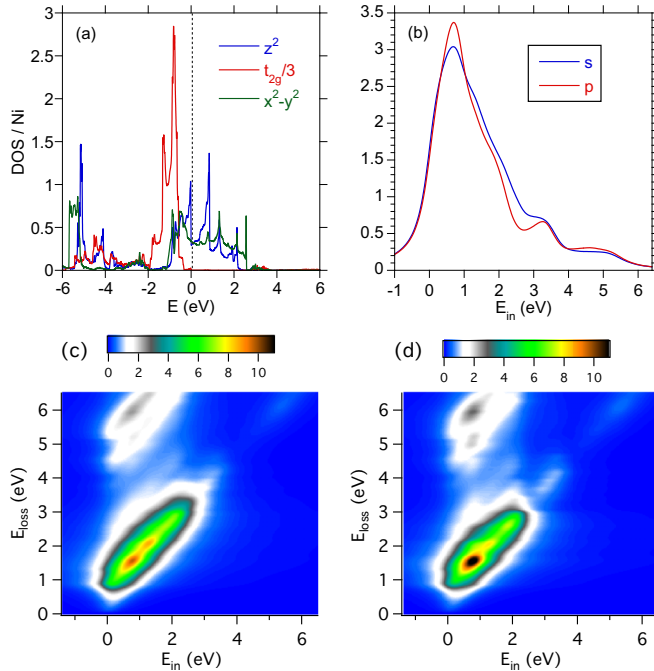


FIG. 8. Density of states for $\text{La}_4\text{Ni}_3\text{O}_{10}$ from DFT (a). Integration of RIXS spectra for $\text{La}_4\text{Ni}_3\text{O}_{10}$ from 4 to 6 eV loss from DFT (b). RIXS spectra for $\text{La}_4\text{Ni}_3\text{O}_{10}$ from DFT for s polarization (c) and p polarization (d) with $\theta = 15^\circ$ and $2\Theta_{sc} = 153^\circ$.

incident energy, that match recent RIXS results for $R_4\text{Ni}_3\text{O}_8$ [6]. We also presented analogous results for $R\text{NiO}_2$, CaCuO_2 , and $R_4\text{Ni}_3\text{O}_{10}$.

Our results, in particular the charge-transfer feature and the dispersive fluorescence line, are a reflection of hybridization of the Ni $3d$ electrons with the oxygen $2p$ ones [25], with an additional contribution from unoccupied $3z^2 - r^2$ states due to their hybridization with the R $5d$ states. The latter plays an important role in certain theories of reduced valence nickelates [26]. Moreover, the strong orbital polarization of the RIXS and XAS spectra, consistent with experiment, is indicative of low-spin d^8 physics for the doped holes. This is due to the dominance of the unoccupied $x^2 - y^2$ weight over that of the $3z^2 - r^2$ weight, as reflected in the DFT and DFT + DMFT density of states.

Given the importance of ultraviolet behavior in determining the underlying microscopic Hamiltonian, we hope our results motivate further RIXS studies of both the reduced nickelates [4–6] as well as cuprates [21], particularly at higher loss energies. More generally, we hope the formalism developed here will be useful in simulating RIXS for a broad range of correlated materials.

ACKNOWLEDGMENTS

J.K., A.J.M., and M.R.N. acknowledge funding from the Materials Sciences and Engineering Division, Basic Energy Sciences, Office of Science, US DOE. Work at the Advanced Photon Source was supported by the US DOE Office of Science, Basic Energy Sciences, under Contract No. DE-AC02-06CH11357. Work at Brookhaven was supported by the US Department of Energy, Office of Science, Office of Basic Energy Sciences, under Award No. DE-SC0022311. H.L. and A.S.B. acknowledge support from NSF Grant No. DMR-2045826 and the ASU Research Computing Center for high-performance computing resources. The Flatiron Institute is a division of the Simons Foundation.

APPENDIX: KRAMERS-HEISENBERG FORMALISM

We start with the Kramers-Heisenberg expression for the RIXS cross section [8,9] in the dipole approximation

$$\tilde{\sigma}(E_{\text{in}}, E_{\text{out}}, \epsilon, \epsilon') = \sum_f \left| \sum_n \frac{\langle f | \epsilon' | n \rangle \langle n | \epsilon | i \rangle}{E_n - E_i - E_{\text{in}} - i\Gamma_n/2} \right|^2 \times \delta(E_{\text{in}} - E_{\text{out}} - E_f + E_i), \quad (\text{A1})$$

where i, n, f are the initial, intermediate, and final states, and Γ_n is the inverse lifetime of the intermediate state. We follow the approach of Ref. [8] that is illustrated in Fig. 1. The RIXS process in the particle-hole approximation involves exciting a $2p$ core electron to an empty $3d$ state, and then having an occupied $3d$ state fill the core hole. As such, $E_n = E' - E_{2p}$ and $E_f = E' - E$, where E' refers to the unoccupied $3d$ states and E to the occupied ones. We then use the δ function to rewrite the energy denominator in Eq. (A1) as $E - E_{2p} - E_{\text{out}} - i\Gamma/2$ where Γ is the core-hole broadening. We now consider the

intermediate state sum by writing the matrix elements as

$$\begin{aligned}
 |\langle n|\epsilon|i\rangle|^2 &= \sum_{k\sigma} \rho_{k,\sigma}(E') |\langle k, \sigma|\epsilon|j\rangle|^2, \\
 |\langle f|\epsilon'|n\rangle|^2 &= \sum_{k\sigma} \rho_{k,\sigma}(E) |\langle k, \sigma|\epsilon'|j\rangle|^2,
 \end{aligned} \quad (\text{A2})$$

where j are the two $2p$ core states for L_2 . We have written the $3d$ states as $|k, \sigma\rangle$ with $k = x^2 - y^2$, etc., and σ is the spin (the angular and spin decomposition of the $3d$ and $2p$ core states are shown in the main text). Summing over the two $2p$ core states, then from Eq. (A1) we arrive at the expressions shown in Eqs. (1) and (2) of the main text:

$$\begin{aligned}
 \tilde{\sigma}(E_{\text{in}}, E_{\text{out}}, \epsilon) &= \sum_{i,f,\sigma,\sigma',\epsilon'} \int dE \rho_{f\sigma'}(E) \rho_{i\sigma}(E + E_{\text{loss}}) \\
 &\times \frac{\Gamma}{2} \frac{M_{if\sigma\sigma'}(\epsilon, \epsilon')}{(E - E_{\text{out}})^2 + \Gamma^2/4},
 \end{aligned} \quad (\text{A3})$$

$$M_{if\sigma\sigma'}(\epsilon, \epsilon') = \left| \sum_j \langle f\sigma'|\epsilon'|j\rangle \langle j|\epsilon|i\sigma\rangle \right|^2, \quad (\text{A4})$$

where $E_{\text{out}} = E_{\text{in}} - E_{\text{loss}}$ and the energy integral (E) is over the occupied $3d$ states ($E' = E + E_{\text{loss}}$). When considering this expression, we note that any core-hole potential shift in the intermediate state has been ignored, and since the zero for E_{in} and E has been set to the Fermi energy, E_{out} then absorbs E_{2p} . As expected, the integrand in the cross section has a resonance when $E = E_{\text{out}}$. Our expression matches Ref. [8], except whereas they approximated the matrix elements by the total $3d$ density of states [their Eqs. (8) and (9)], we instead keep the full angular dependence by using the orbitally resolved density of states. That way, we properly account for the polarization factors associated with the transitions between the $2p$ core states and the $3d$ conduction/valence states.

-
- [1] D. Li, K. Lee, B. Y. Wang, M. Osada, S. Crossley, H. R. Lee, Y. Cui, Y. Hikita, and H. Y. Hwang, Superconductivity in an infinite-layer nickelate, *Nature (London)* **572**, 624 (2019).
- [2] J. Zaanen, G. A. Sawatzky, and J. W. Allen, Band Gaps and Electronic Structure of Transition-Metal Compounds, *Phys. Rev. Lett.* **55**, 418 (1985).
- [3] Y. Shen, J. Sears, G. Fabbris, J. Li, J. Pellicciari, I. Jarrige, X. He, I. Božović, M. Mitrano, J. Zhang, J. F. Mitchell, A. S. Botana, V. Bisogni, M. R. Norman, S. Johnston, and M. P. M. Dean, Role of Oxygen States in the Low Valence Nickelate $\text{La}_4\text{Ni}_3\text{O}_8$, *Phys. Rev. X* **12**, 011055 (2022).
- [4] M. Hepting, D. Li, C. J. Jia, H. Lu, E. Paris, Y. Tseng, X. Feng, M. Osada, E. Been, Y. Hikita, Y.-D. Chuang, Z. Hussain, K. J. Zhou, A. Nag, M. Garcia-Fernandez, M. Rossi, H. Y. Huang, D. J. Huang, Z. X. Shen, T. Schmitt *et al.*, Electronic structure of the parent compound of superconducting infinite-layer nickelates, *Nat. Mater.* **19**, 381 (2020).
- [5] M. Rossi, H. Lu, A. Nag, D. Li, M. Osada, K. Lee, B. Y. Wang, S. Agrestini, M. Garcia-Fernandez, J. J. Kas, Y.-D. Chuang, Z. X. Shen, H. Y. Hwang, B. Moritz, K.-J. Zhou, T. P. Devereaux, and W. S. Lee, Orbital and spin character of doped carriers in infinite-layer nickelates, *Phys. Rev. B* **104**, L220505 (2021).
- [6] Y. Shen, J. Sears, G. Fabbris, J. Li, J. Pellicciari, M. Mitrano, W. He, J. Zhang, J. F. Mitchell, V. Bisogni, M. R. Norman, S. Johnston, and M. P. M. Dean, Electronic Character of Charge Order in Square-Planar Low-Valence Nickelates, *Phys. Rev. X* **13**, 011021 (2023).
- [7] Experimentally, this zero can be determined from the midpoint of the leading edge of the XAS.
- [8] J. Jiménez-Mier, J. van Ek, D. L. Ederer, T. A. Callcott, J. J. Jia, J. Carlisle, L. Terminello, A. Asfaw, and R. C. Perera, Dynamical behavior of x-ray absorption and scattering at the L edge of titanium compounds: Experiment and theory, *Phys. Rev. B* **59**, 2649 (1999).
- [9] A. Hariki, M. Winder, and J. Kuneš, Continuum Charge Excitations in High-Valence Transition-Metal Oxides Revealed by Resonant Inelastic X-Ray Scattering, *Phys. Rev. Lett.* **121**, 126403 (2018).
- [10] N. Binggeli and M. Altarelli, Orbital ordering, Jahn-Teller distortion, and resonant x-ray scattering in KCuF_3 , *Phys. Rev. B* **70**, 085117 (2004).
- [11] V. N. Antonov, D. A. Kukusta, and L. V. Bekenov, Electronic structure and resonant inelastic x-ray scattering in osmates. I. Perovskite NaOsO_3 , *Phys. Rev. B* **105**, 155144 (2022).
- [12] A. S. Botana and M. R. Norman, Similarities and Differences between LaNiO_2 and CaCuO_2 and Implications for Superconductivity, *Phys. Rev. X* **10**, 011024 (2020).
- [13] A. S. Botana, V. Pardo, W. E. Pickett, and M. R. Norman, Charge ordering in $\text{Ni}^{1+}/\text{Ni}^{2+}$ nickelates: $\text{La}_4\text{Ni}_3\text{O}_8$ and $\text{La}_3\text{Ni}_2\text{O}_6$, *Phys. Rev. B* **94**, 081105(R) (2016).
- [14] J. Zhang, D. Phelan, A. S. Botana, Y.-S. Chen, H. Zheng, M. Krogstad, S. G. Wang, Y. Qiu, J. A. Rodriguez-Rivera, R. Osborn, S. Rosenkranz, M. R. Norman, and J. F. Mitchell, Intertwined density waves in a metallic nickelate, *Nat. Commun.* **11**, 6003 (2020).
- [15] J. Karp, A. S. Botana, M. R. Norman, H. Park, M. Zingl, and A. Millis, Many-Body Electronic Structure of NdNiO_2 and CaCuO_2 , *Phys. Rev. X* **10**, 021061 (2020).
- [16] J. Karp, A. Hampel, M. Zingl, A. S. Botana, H. Park, M. R. Norman, and A. J. Millis, Comparative many-body study of $\text{Pr}_4\text{Ni}_3\text{O}_8$ and NdNiO_2 , *Phys. Rev. B* **102**, 245130 (2020).
- [17] J. Zhang, Y.-S. Chen, D. Phelan, H. Zheng, M. R. Norman, and J. F. Mitchell, Stacked charge stripes in the quasi-2D trilayer nickelate $\text{La}_4\text{Ni}_3\text{O}_8$, *Proc. Natl. Acad. Sci. USA* **113**, 8945 (2016).
- [18] J. Zhang, A. S. Botana, J. W. Freeland, D. Phelan, H. Zheng, V. Pardo, M. R. Norman, and J. F. Mitchell, Large orbital polarization in a metallic square-planar nickelate, *Nat. Phys.* **13**, 864 (2017).
- [19] To compare experiment to theory, we determined the experimental zero of the incident energy axis by integrating the RIXS spectra over loss energy, which is an approximation to the XAS, and then fit the leading edge to a Fermi function. To compare the intensity scales, we based the experimental scale on the non d - d excitation part of the spectra, since the d - d excitations are not present in the theory.

- [20] K. Higashi, M. Winder, J. Kuneš, and A. Hariki, Core-Level X-Ray Spectroscopy of Infinite-Layer Nickelate: LDA+DMFT Study, *Phys. Rev. X* **11**, 041009 (2021).
- [21] B. W. Lebert, M. P. M. Dean, A. Nicolaou, J. Pellicciari, M. Dantz, T. Schmitt, R. Yu, M. Azuma, J.-P. Castellán, H. Miao, A. Gauzzi, B. Baptiste, and M. d'Astuto, Resonant inelastic x-ray scattering study of spin-wave excitations in the cuprate parent compound $\text{Ca}_2\text{CuO}_2\text{Cl}_2$, *Phys. Rev. B* **95**, 155110 (2017).
- [22] For cuprates, the $d-d$ excitations are so dominant, the charge-transfer and fluorescence line features in Ref. [21] required a log intensity scale to become apparent.
- [23] Although $\text{La}_4\text{Ni}_3\text{O}_{10}$ is orthorhombic, to ease comparison to the other cases, our DFT input was generated from an optimized $I4/mmm$ structure.
- [24] G. Fabbri, D. Meyers, Y. Shen, V. Bisogni, J. Zhang, J. F. Mitchell, M. R. Norman, S. Johnston, J. Feng, G. S. Chiuzbăian, A. Nicolaou, N. Jaouen, and M. P. M. Dean, Resonant inelastic x-ray scattering data for Ruddlesden-Popper and reduced Ruddlesden-Popper nickelates, *Scientific Data* **10**, 174 (2023).
- [25] H. LaBollita and A. S. Botana, Electronic structure and magnetic properties of higher-order layered nickelates: $\text{La}_{n+1}\text{Ni}_n\text{O}_{2n+2}$ ($n = 4-6$), *Phys. Rev. B* **104**, 035148 (2021).
- [26] K. Foyevtsova, I. Elfimov, and G. A. Sawatzky, Electride-like properties of infinite-layer nickelates [arXiv:2208.14556](https://arxiv.org/abs/2208.14556).